Title

Calcite veins as an indicator of fracture dilatancy and connectivity during strike-slip faulting in Toarcian shale (Tournemire tunnel, Southern France)

Authors

Lefèvre, Mélody
Guglielmi, Yves
Henry, Pierre
et al.

Publication Date

2016-02-01

DOI

10.1016/j.jsg.2016.01.002

Peer reviewed

Calcite veins as an indicator of fracture dilatancy and connectivity during strike-slip faulting in Toarcian shale (Tournemire tunnel, Southern France)

Author links open overlay panelMélodyLefèvre[a]YvesGuglielmi[a]PierreHenry[a]PierreDick[b]ClaudeGout[c]
Show more

https://doi.org/10.1016/j.jsg.2016.01.002Get rights and content

Highlights

- Cathode-luminescence observations indicate that two phases of vein formation occurred.
- Fluids circulations mainly off the shear surfaces in centimeter scale dilatant volumes.
- Relationships between calcite concentration and strain partition around the fault main slip surface.

Abstract

The reactivation of faults induced by natural/human induced fluid pressure increases is a major concern to explain subsurface fluid migration and to estimate the risk of losing the integrity of reservoir/seal systems. This study focusses on paleo-fluid migration in a strike slip fault with >100 m long, affecting a Toarcian shale (Causses Basin, France). A high calcite concentration is observed in a 5 cm thick zone at the boundary between the fault core and damage zone. Cumulated displacements in this zone are of millimeter-to-centimeter-scale offsets and different dilatant deformation textures are observed. The zone is affected by thin slip planes containing gouge. Cathodo-luminescence observations indicate that two phases of vein formation occurred. The first phase coincides with the fluid migration along this centimeter thick dilatant zone. The second one is associated to re-shear along the millimeter thick slip planes that results in more localized mineralization, but also in a better hydrologic connection through the shale formation. These results show that in shales fluids may migrate off a slipping surface in centimeter scale dilatant volumes, at first controlled by the intact

shale anisotropy related to bedding and then favored by brecciating, structures re-orientation and strengthening processes induced by calcite sealing effects.

- **Previous** article in issue
- **Next** article in issue

Keywords

Shale
Fault activation
Paleo-fluids migration
Seal
Vein geochemistry

1. Introduction

Fluid pressurization effects on the re-activation of faults affecting shale formations are a crucial process to understand fluid migration through seal layers, eventually producing loss of the reservoir/seal systems integrity. The reservoir/seal system integrity is of key prime importance for many applied domains (oil and gas extraction, storage site of radioactive waste/CO_2, geothermal projects…).

It is commonly admitted that a fault cannot be considered as a single continuous surface but corresponds to a rock volume having various deformation structures on different scales of space and intensity (Gudmundsson et al., 2001, Constantin et al., 2004, Faulkner et al., 2010, Gudmundsson et al., 2001). Typically, a fault zone is composed of a core surrounded by a damage zone consisting of a transitional zone between the core and the intact host rock (Caine et al., 1996, Chester et al., 1993, Wibberley et al., 2008, Faulkner et al., 2010) or multiple fault cores (Faulkner et al., 2003). The fault core/damage zone boundary sometimes is gradual, but more often appears as a sharp interface interpreted as a fault plane. The fault core is composed of various structures such as slip surface planes, breccia, gouge, cataclasite, ultra-cataclasites, mylonites and ultra-mylonite (Sibson, 1977, Chester and Logan, 1986, Chester et al., 1993, Bruhn et al., 1994, Caine et al., 1996, Clausen et al., 2003, Kim et al., 2004). Structures observed in the damage zone are fractures, subsidiary faults, veins, folds and cleavages (Chester and Logan, 1986, Chester et al., 1993, Caine et al., 1996, Hesthammer et al., 2000, Jourde et al., 2002, Berg and Skar, 2005).

Such structural heterogeneity of fault zones induces strongly heterogeneous fluid flow in the fault zone (Evans et al., 1997, Mandl et al., 1977, Manzocchi et al., 1999, Yielding

et al., 1999). The intensification of the fracture network in the damage zone may lead to an increased permeability with respect to less fractured zone (Caine et al., 1996, Faulkner et al., 2010, Gudmunson et al., 2010). Fault core, contain specific grain size reducing structures (Billi et al., 2003) that generally result in decreasing permeability. On the other hand, during shear movement on the fault, dilatant effects may favor permeability increase, which in return may influence the evolution of fault slip (Rice and Rudnicki, 1979).

In fault zones affecting shale formations, self-healing of fractures and sealing with calcitecement, limits the permeability increase of both the damage and core zones (Constantin et al., 2004, Nussbaum et al., 2011). Other processes than grain size reduction can influence the permeability of the fault core, such as mineral reorientation (Charpentier et al., 2003, Constantin et al., 2007, Arch and Maltman, 1990). Laboratory experiments on clay rich fault cores show that, for a given porosity and effective stress, shearing generally results in permeability decrease both along and across the shear zone (Wibberley et al., 2008). For these reasons, shale faults are considered to have a low permeability in the same order as that of the intact rock (Nussbaum and Bossart, 2004). However, porosity and permeability can increase when the stress path applied to the sample results in a dilatant behavior (Zhang and Cox, 2000). Moreover, the concentration of calcite veins in fault zones suggest that fluid migration can occur during fault activation or movement. The key question is under which stress/strain processes the permeability does increase during faulting in shales. This study investigates the relationships between structural deformations and calcite crystallizations close to the main slipping surface at the interface between the damage zone and the fault core, of a pluri-hectometre reverse-strike slip fault affecting the Toarcian shales in the Tournemire Underground Research Laboratory (URL, France). The aim is to identify processes causing permeability increase during faulting in shale that include dilatancyoccurring off the main slipping plane.

2. Fault geology in the Tournemire URL and paleo-fluid circulations

The Tournemire Underground Research Laboratory (URL) located in the Mesozoicsedimentary basin of the French Causses (Massif Central, France, Fig. 1), is operated by the French Institute for Radiological Protection and Nuclear Safety (IRSN), to study the confining properties of an argillaceous formation (Cabrera et al., 1999, Boisson et al., 2001). The URL is nested in a monoclinal structure tilted 5°–10° to the North (Constantin et al., 2004) in a 250 m thick shale formation respectively composed of 50 m thick Domerian and 200 m thick Toarcian series intercalated

between two 300–500 m thick dolomitic limestonelayers of Bathonien-Bajocian-Aalenian ages and Carixian-Sinemurian ages (Cabrera et al., 1999) (Fig. 1). The shale's mineral composition is relatively homogeneous within the upper Toarcian section, with more than 50 wt.% clay minerals, dominantly illite and illite/smectite, 10–20 wt.% calcite, and 10–20 wt.% quartz. Other components (less than 10 wt.%) include detrital micas, feldspars, pyrite and Fe-dolomite, and organic matter (Boisson et al., 2001, Tremosa et al., 2012). The shale formation has a porosity of 10 –13%, (Dick et al., 2015) a water content of 4–6 wt.% and a hydraulic permeability of 10^{-14}–10^{-15} m/s (10^{-21}–10^{-22} m^2) in the laboratory and of 10^{-11}–10^{-14} m/s (10^{-18}–10^{-21} m^2) in situ (Bonin, 1998, Boisson et al., 2001, Cabrera et al., 1999, Courbet et al., 2013).

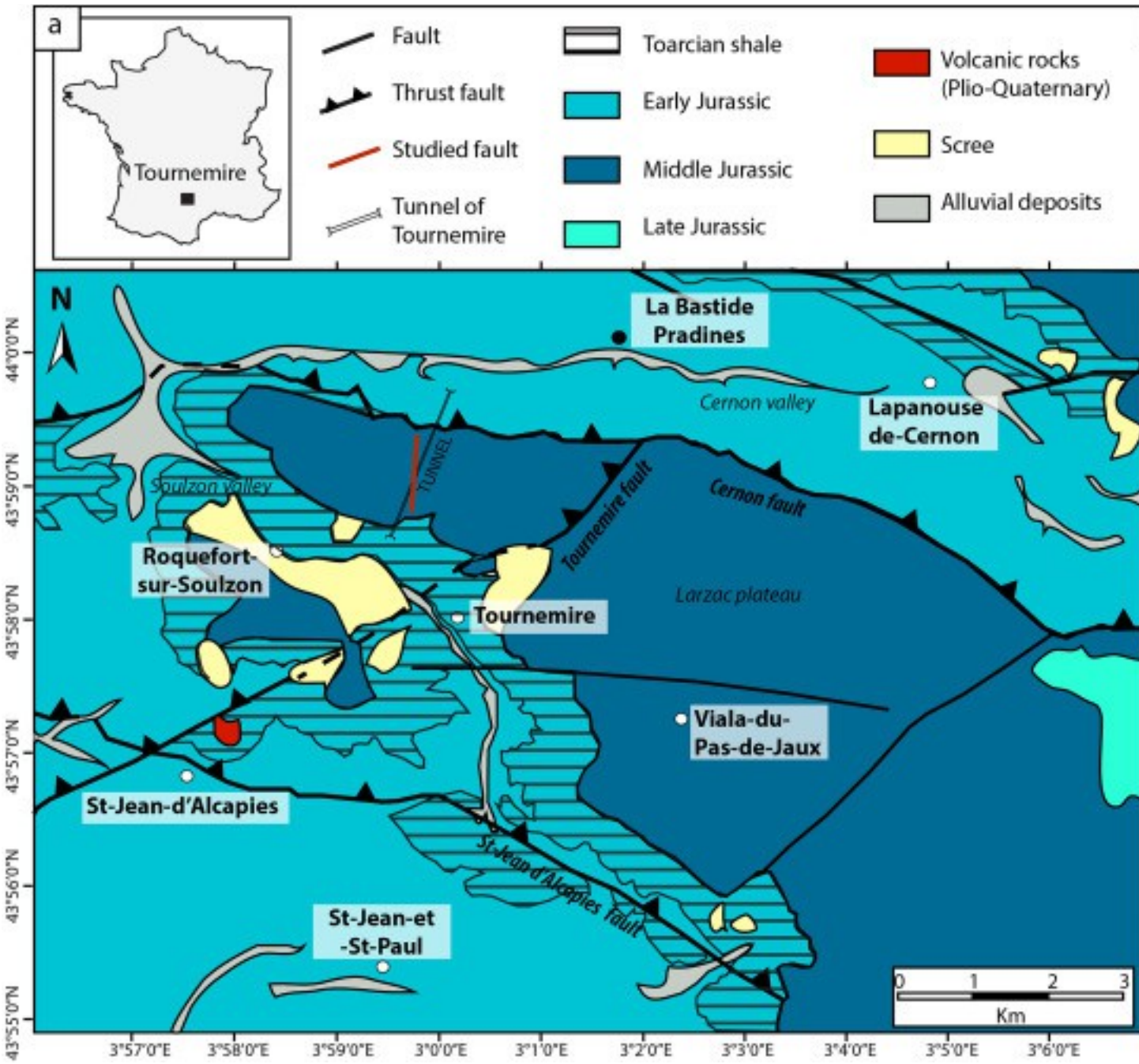

1. Download high-res image (1MB)
2. Download full-size image

Fig. 1. a- Geological map, the studied fault is indicated in red. b- Simplified stratigraphic log (l1-2, Hettengian; l3-4, Sinemurian; l5, Carixian; l6, Domerian; l7, Early Toarcian; l8-9a, Late Toarcian-Early Aalenian; l9b, Late Aalenian; j1a, Early Bajocian; j1b, Late Bajocian; j2a, Early Bathonian; j2b, Late Bathonian; j3-5, Callovian-Early Oxfordian and j6-7 Late Oxfordian-Early Kimmerigdian). (For interpretation of the references to colour in this figure legend, the reader is referred to the web version of this article).

The URL is crossed by two main parallel fault zones (F1 and F2) separated by relatively undeformed rock (Bretaudeau et al., 2014). The location and the geometry of the fault zones were reconstructed using boreholes previously drilled by IRSN and by mapping the intersections between the faults and the URL galleries' walls (Fig. 2). Both faults (F1 and F2) have a similar dip and dip-direction spatially varying from N170°–N010°; 60°–90°W (Fig. 2), characterized by left-lateral strike slip movement with a reverse component (Peyaud et al., 2006). Some small (meter-to-decameter long) N130°–N150° faults connect F1 and F2 (Constantin, 2002, Bretaudeau et al., 2014). Faults F1 and F2 are crossing a tectonic block bounded to the North by the N090° Cernon fault, to the South by the N090° St Jean d'Alcapies fault and the N040° Tournemire fault (Fig. 1) (Constantin et al., 2004). These three faults extend into the basement and are considered to be inherited structures from the Hercynian orogeny (De Charpal et al., 1974, Bonijoly and Delpont, 1982).

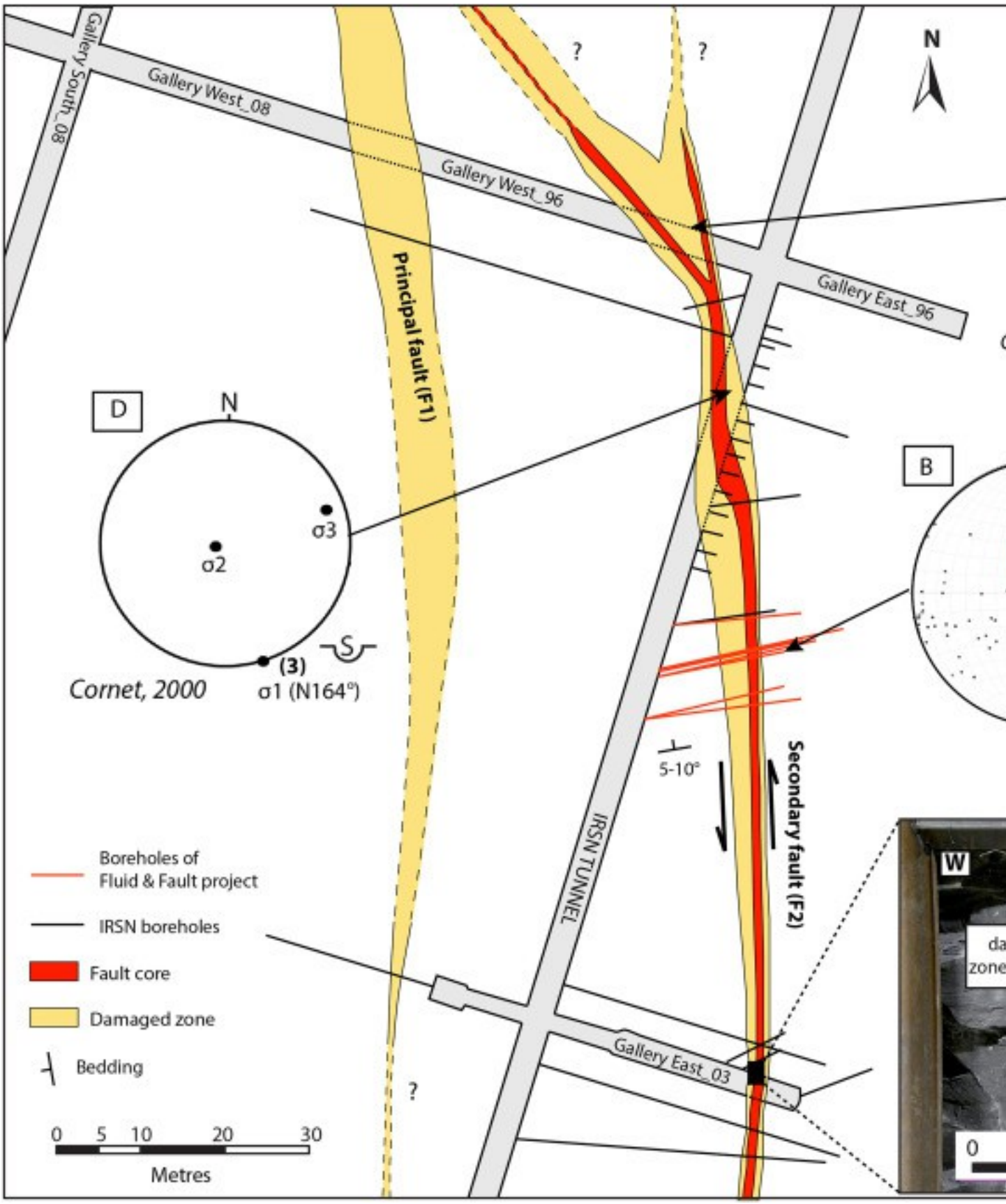
Gallery South_08
Gallery West_08
Gallery West_96
Gallery East_96
Gallery East_03
Principal fault (F1)
Secondary fault (F2)
IRSN TUNNEL
N
D
σ3
σ2
(3)
σ1 (N164°)
Cornet, 2000
B
5-10°
Boreholes of Fluid & Fault project
IRSN boreholes
Fault core
Damaged zone
Bedding
0 5 10 20 30
Metres
W
0

1. Download high-res image (1MB)
2. Download full-size image

Fig. 2. IRSN URL structural map (F1 and F2); A- Picture of the principal fault plane (N0°-N170°; 80°–90°W) at the boundary between the western compartment of the damage zone (FDZW) and the fault core (FC), in the Gallery East_03. The black rectangle shows the block sample location (Fig. 3). B) Poles of fracture and fault planes were determined on the image of borehole walls and from core analyses of Fluid & Fault project boreholes drilled from the tunnel. C) Paleo-stress orientation determined by slickensidesanalyses in Gallery West_96 (Constantin, 2002). D) Actual tensor orientation determined by leak off tests (Cornet, 2000).

Two main tectonic stress regimes have affected the Causses basin. An extension during the Upper Jurassic and the Lower Cretaceous (Blès et al., 1989, Martin and Bergerat, 1996, Constantin et al., 2002), characterized by σ_3 oriented N–S was followed by a Mid-Cretaceous to Eocene Pyrenean compression during which σ_1 varied from NE/SW to NW/SE, with two main pulses striking N020°–N030° and N160°–N170°. (Constantin et al., 2002, Constantin et al., 2004). The Cernon and the St Jean d'Alcapies faults were reactivated as normal faults during the Mesozoic extension and as reverse faults during the Pyrenean compression. These faults display a cumulative vertical inverse offset of 100–400 m (Constantin et al., 2002). F1 and F2 faults presumably are associated to the compressive Pyrenean tectonic phase. Consequently, these faults may have activated as a right lateral strike-slip during the first compressive pulse, and a left-lateral ones during the second (or last) pulse. Left lateral strain features appear more developed in the fault zone, Constantin (2002) determined a σ_1 oriented N134° from microstructural analyses conducted in the northern part of the fault zone (Fig. 2C). However, this principal stress direction has not been found outside the Tournemire URL, and could result from local stress rotation during the faulting process associated to the N160° tectonic episode (Constantin, 2002). The analysis of calcite twins on several veins in fault zones in the studied area (1 km^2 around the Tournemire URL, Fig. 1), Constantin et al. (2007) estimated that the paleo-deviatoric stress (σ_1–σ_3) at the onset of the Pyrenean tectonic inversion was ≥40–50 MPa.

In order to determine the burial depth of the Toarcian shales during the Pyrenean compression period, Séranne (2014) have reconstructed a subsidence curve based on data from Barbarand et al., 2001, Séranne et al., 2002, Peyaud et al., 2005. This gives a range of maximal burial depths of 2.3–2.4 km roughly corresponding to burial stresses of 57–62 MPa at the onset of the Basin inversion, and at the potential activation time of the studied fault. Thus an estimated magnitude range of paleostress tensor's can be

inferred from the principal stresses applied on the studied fault considering a strike slip regime with a sub-horizontal σ_1 > 70 MPa, a sub-vertical σ_2 ~ 60 MPa and a sub-horizontal σ_3 ~ 30–40 MPa.

One should note that the present day stress tensor orientation determined with a series of leak-off tests performed in a vertical 180 m deep borehole (Cornet, 2000) is identical to the paleostress tensor's orientation during the second Pyrenean pulse, revealing a "residual" strike slip regime on the studied fault (Fig. 2D). At the URL depth, stress magnitudes are characterized by σ1 = 4 ± 2 MPa, horizontal and oriented N162°±15°E, σ2 = 3.8 ± 0.4 MPa, 7–8° inclined from vertical in the N072° direction and σ3 = 2.1 ± 1 MPa, 7–8° inclined from horizontal in the N072° direction (Fig. 2C). We may thus consider that this state of stresses has been at steady-state since the end of the uplift period at the Eocene times.

Previous studies (Peyaud et al., 2006) of carbon and oxygen isotopic composition of carbonates from the Tournemire URL highlighted two fluid sources: formation fluids contained in veins affecting the intact Toarcian formation (same composition than the shale cement) and meteoric fluids that influence the composition of veins in the main fault zones (and in a meter size alteration halo around the fault). In the fault zones, some mobility of iron, zinc and REE (rare earth element) was also reported. Peyaud et al. (2006) observed that pyrite recrystallization is associated with early calcite cements, which iron content may exceed 1%, indicating reducing conditions prevailed despite of some meteoric water input. Zoned calcite filling in some geodes indicates fluctuating redox conditions, episodic connections with the overlying Aalenian aquifer, and an evolution in time toward a more open hydrogeologic system (Peyaud et al., 2006).

The fault zone studied in this paper (F2) is >100 m long and the vertical offset is estimated to be 4–5 meters (Dick et al., 2015). The total thickness of the damage zone (footwall and hanging wall) varies spatially between 9 and 15 m depending on the location (estimations were conducted in borehole figured in red in Fig. 2). The damage zone thickness in the hanging wall (west fractured damage zone; FDZW) is about three times that in the footwall (east fractured damage zone; FDZE). While in the Gallery East_03 (Fig. 2), the FDZW and the FDZE roughly have the same thickness. Different fracture and fault orientations characterize the FDZ (Figs. 2A and B); with main directions respectively trending N40°–N90° and dipping 10°–90° NW or SW: N160°–N020° dipping 20°–90° W, and N160°–N170° dipping 75°–90°W (Constantin, 2002). Image of borehole (in red in Fig. 2) walls obtained by the well logging system OPTV (borehole optical televiewer probe) and cores were used for the geological

structures analysis. 10–20% of fractures are parallel or close to bedding. Most of the other fractures (>70%) display a dominant strike of N160°–N020° with large dip variations (Fig. 2B). Subvertical planes oriented N160°–N020° often expose slickenlines indicating strike-slip motion. The two first direction families display large calcite fillings and some geodes (Peyaud et al., 2006), while the third one is characterized by polished striated planes.

In the studied zone, the fault core (FC) is 0.1–2.4 m thick. It displays a structural heterogeneity characterized by centimeters thick shear zones filled with gouge material bounded by 0.1–0.2 m thick highly fractured zones as well as lenses of intact shale. The main orientation of the shear zones follows the N170°–N010°; 80°W average orientation of the fault (Fig. 2A). Millimeter to centimeter thick calcite veins are observed at the FDZW/FC boundary.

3. Methodology

In this paper, we describe a detailed study of calcite veins localized at the boundary between the damage zone and the fault core of F2 fault (Fig. 2). This interface is fragile, thus when drilling the boundary between the damage zone and the fault core is systematically damaged and only poor quality samples can be recovered. The gallery_03 and gallery_96 walls are the only places where this interface is exposed for favorable sampling conditions. The studied sample comes from the gallery_03 where the fault's architecture is more simple compared to gallery_96 where two fault cores are observed. Neither the less similar calcite structures are observed in the two galleries. We have sampled a 12 cm × 8 cm × 8 cm block (Fig. 2, Fig. 3). The block was sealed in epoxy resin before being CT-scanned to avoid any fracturing induced by shale desiccation. A microstructural study was then conduced on polished vertical and horizontal sections. Then, the block was cut into a series of thirteen 22 × 22 × 22 mm cubes, which were analyzed by cathodo-luminescence (CL) on thin sections; three of the cubes were analyzed by micro X-ray Fluorescence (μXRF). The μXRF is an effective method to perform semi-quantitative chemical non-destructive micro-analyses and chemical mapping with 2D high spatial resolution (10–100 μm) (Devès et al., 2012).

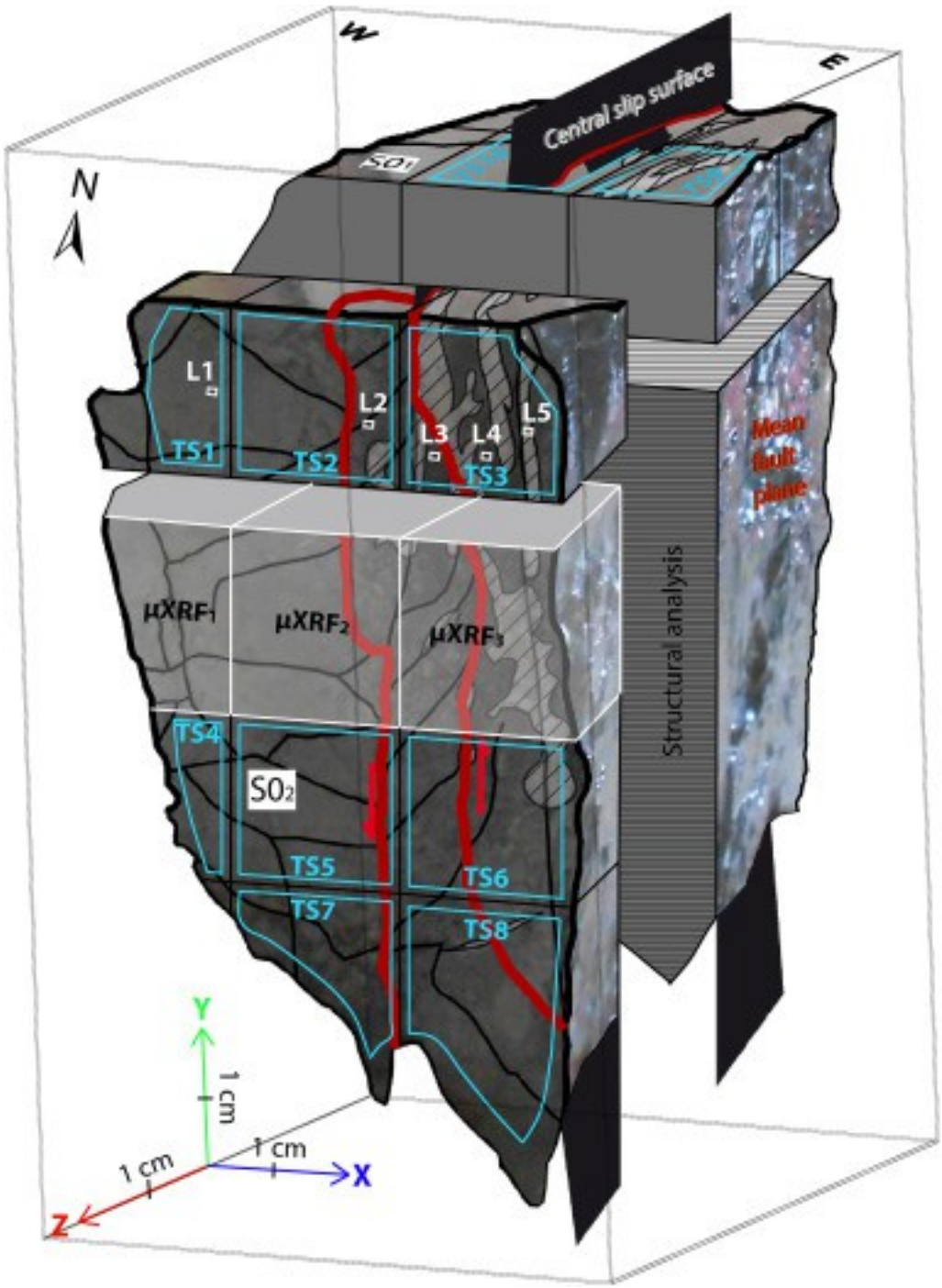

1. Download high-res image (852KB)
2. Download full-size image

Fig. 3. Studied block sample (Location in Fig. 2A). Grey hatched block vertical and horizontal surfaces were subjected to a microstructural study presented in Fig. 4. Contoured blue areas (TS1, TS2, TS3, TS4, TS5, TS6, TS7, TS8, TS9 and TS10) represent thin sections locations. White rectangles (L1, L2, L3, L4 and L5) represent the locations of the thin sections photographs presented in Fig. 5. White cubes

(μXRF$_1$, μXRF$_2$ and μXRF$_3$) represent μXRF analyzed zones presented in Fig. 8. S01 and S02 represent location of stratigraphic plane measurement presented in Fig. 4. (For interpretation of the references to colour in this figure legend, the reader is referred to the web version of this article).

The μXRF is operated on an X-ray analytical microscope (XGT-7000) combining micro-X-ray fluorescence with X-ray microscopy. The XGT-7000 consists of an excitation source, a parabolic capillary and an Energy Dispersive Sensor (EDS) detector. The excitation source of the XGT-7000 is an X “primary” ray (XR) produced by an X-ray tube equipped with an anode of rhodium (Rh) to which is applied a voltage of 30 kV.

The parabolic capillary provides a 10 μm diameter very intense (10^8 photons/s) incident XR beam which “excites” the atoms in the sample in order to generate an X fluorescence emission spectrum. Under the influence of X-rays, electrons can be torn from the energy level on which they are located. The free place is then likely to be filled by electrons located at a higher energy level. These substitutions are accompanied by photon emissions (fluorescence radiation) collected by an EDS detector. This detector can quickly and simultaneously detect a wide energy band of the X fluorescence emitted by several elements (U–Na). Intensities of radiation-emitted fluorescence are proportional to the number of excited atoms and wavelengths (energy) being characteristic of these atoms.

Eight polished thin sections (3 from the eastern compartment adjacent to the main fault plane displaying a higher intensity of deformation and 5 from the western fractured compartment, TS1 to TS8, Fig. 3) were examined by optical microscopy and cathodo-luminescence. A Technosyn Cold Cathode Luminescence Model 8200 Mk II is attached to an Olympus™ BH2 microscope and to a Zeiss™ MRc5 digital camera in order to compare the results from optical microscopy and CL. The main purpose is to provide information on the distribution of the calcite and sulphides phase in the microstructures.

4. Results

4.1. Shear induced dilation at the FDZ/FC transition zone inferred from microstructural analyses

The sampled block may be divided in two: (i) a western fractured compartment and (ii) an eastern compartment adjacent to the main slickenlined fault surface that bounds the block (eastern extremity of sample, Fig. 3). The eastern compartment displays a higher deformation intensity. The boundary between the two corresponds to a shear surface (Fig. 3, Fig. 4). In the western compartment, an increase of the bedding dip is observed from horizontal at the block west boundary to 35°SE close to the central slip surface

(stereo in Fig. 4 and $S0_1$ and $S0_2$ locations in Fig. 3). In the eastern compartment, the bedding is strongly deformed, and only preserved into centimeter-thick zones.

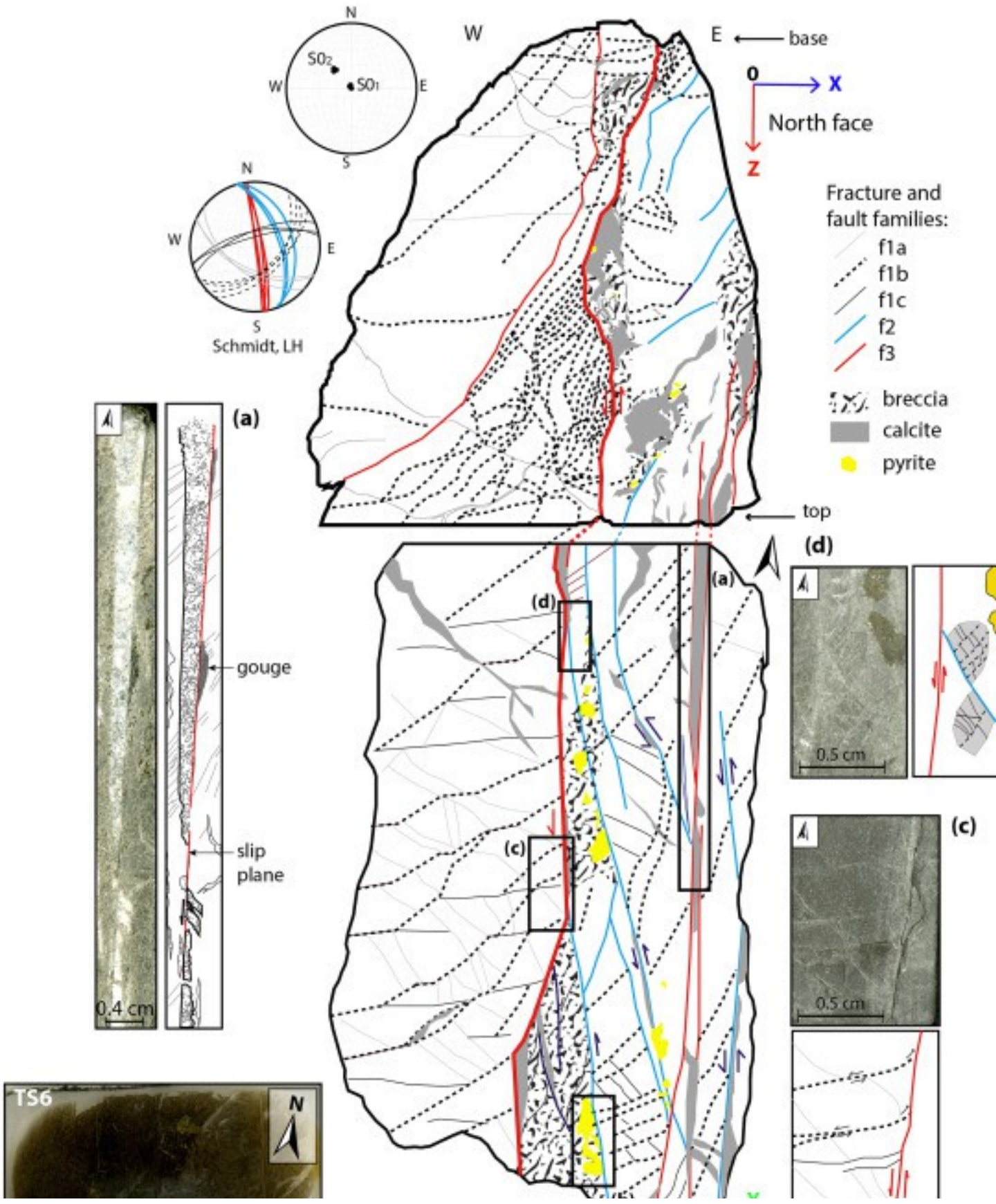
N
W
E
S
SO2
SO1
Schmidt, LH
W
E
base
0
X
North face
Z
Fracture and fault families:
f1a
f1b
f1c
f2
f3
breccia
calcite
pyrite
top
(a)
gouge
slip plane
0.4 cm
(d)
(c)
0.5 cm
TS6
N

1. Download high-res image (3MB)
2. Download full-size image

Fig. 4. Structural analyses of vertical (0zx) and horizontal (0xy) surfaces perpendicular to the principal fault plane direction (location in Fig. 3). Grey lines, dashed dark and black lines represent family 1a, 1b and 1c fractures (f1a, f1b and f1c), blue lines and red lines represent family 2 and 3 fractures (f2 and f3), respectively. a- Details of a slip plane zone. b- Details of a brecciated zones cemented with calcite. c- Zoom of anticlockwise rotation and a left-lateral strike slip of family 1 faults close to left-lateral strike family 3 faults. d- Zoom of left-lateral strike slip of family 2 faults indication. e- and f- Details of sigmoidal veins of f1b fault observed in TS6 and TS8 thin sections, respectively (location in Fig. 3). g- (Pol) is the observation with a polarizing microscope and (CL) are the cathodo-luminescence observations (location in Fig. 4e). S01 and S02 represent stratigraphic plane measurement (location in Fig. 3). (For interpretation of the references to colour in this figure legend, the reader is referred to the web version of this article).

The block is affected by five geometric faults families (f1a, f1b, f1c, f2 and f3):

- Families f1a, f1b and f1c (thin grey continuous lines, dashed dark lines and black continuous lines in Fig. 4) correspond to faults N110°–N130°, dipping 55°–65°SW; N030°–N060°, 45°–60°SE and N060°–N080°, 60°–80°N. Towards the East, the faults are cut by f2 and f3 faults, both strike and dip were rotated anticlockwise, respectively to N30° and >60°–80° dip. f1a, f1b and f1c faults are mostly observed in the western part of the block where they entirely cut the block (Fig. 4). They are less observed in the eastern part of the block. Sigmoidal veins indicating a dextral movement are observed on f1b fault (Fig. 4e–f), and an anticlockwise rotation and a left-lateral strike slip reactivation (Fig. 4c) are observed on f1b and f1c faults close to f3 faults. The apparent offsets are small (a few mm at most).
- f2 (blue lines in Fig. 4) corresponds to left-lateral strike slip faults N150°–N160° dipping 60°–80° to the E. These faults are mainly located in the eastern part of the block (Fig. 4d). They do not cut the entire block and branch on to the f3 fault surfaces. They may be considered as Riedel R1-shear planes associated to f3 shear planes during the second compression episode, oriented NW–SE.
-

f3 (red lines in Fig. 4) corresponds to strike slip faults N170°–N180° dipping 80°–90° to the E or W (Fig. 4c). A left lateral movement is observed with a small vertical component characterized by slikenslides dipping 10°–20°N. This family includes the main slickenlined fault surface, the central fault surface bounding the two compartments, and several (4–5) faults located within the eastern compartment of the block. The minimum offset estimated from the displacement of small calcite shear veins along each plane is several centimeters, thus the total slip on the fault surface may in fact exceed block's length (>5 cm, Fig. 4 and a).

Compared with the western block compartment, the eastern one displays a higher intensity of deformation characterized by brecciated zones composed of shale material elements cemented with large amounts of calcite intercalated with deformed shale (Fig. 4b) where the bedding appears rotated anticlockwise. Thin discontinuous black bands (no calcite, Fig. 6b) show, strong deformation looking like gouge material and calcite shear veins are observed along several f3 slip planes (Fig. 4, Fig. 6b). Along the central slip plane, at the branching with the f2 faults, centimeter-thick breccia made of shale and fractured pyrite elements cemented with calcite are observed (Fig. 4b), these cemented breccia thus formed during left-lateral strike-slip motion. In these local highly dilatant zones, the breccia displays poorly matrix-supported to cement-supported textures.

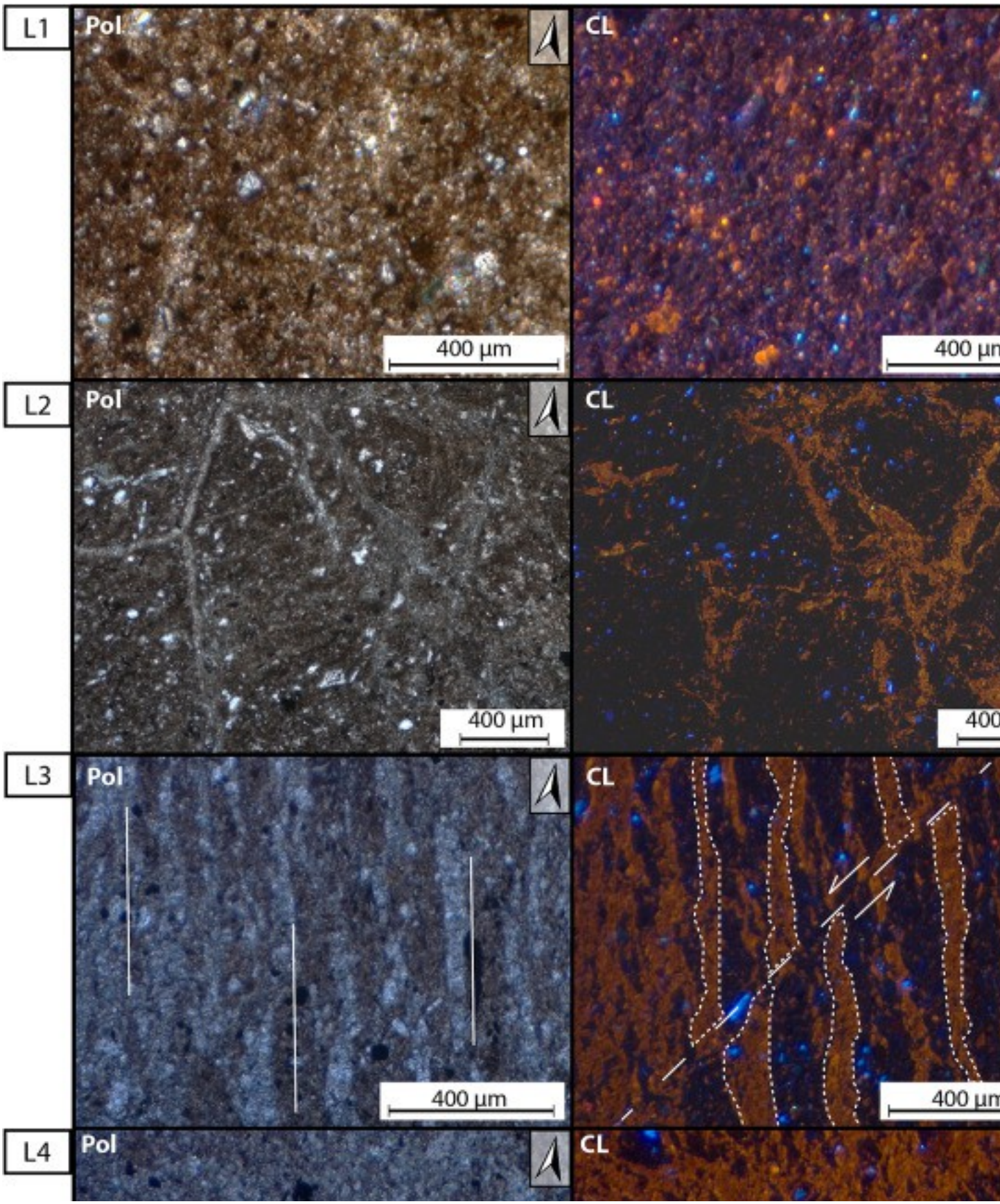
L1
Pol
CL
400 µm
L2
Pol
CL
400 µm
L3
Pol
CL
400 µm
L4
Pol
CL

1. Download high-res image (2MB)
2. Download full-size image

Fig. 5. Thin sections of different fault zone materials. For each thin section, (Pol) is the observation with a polarizing microscope and (CL) is the cathodo-luminescence observation. L1, L2 analyzed zones are localized in the FDZW (in TS1 and TS2 thin sections, Fig. 3) and L3, L4 and L5 are localized in the DZ/FC transition zone (in TS3 thin section, Fig. 3).

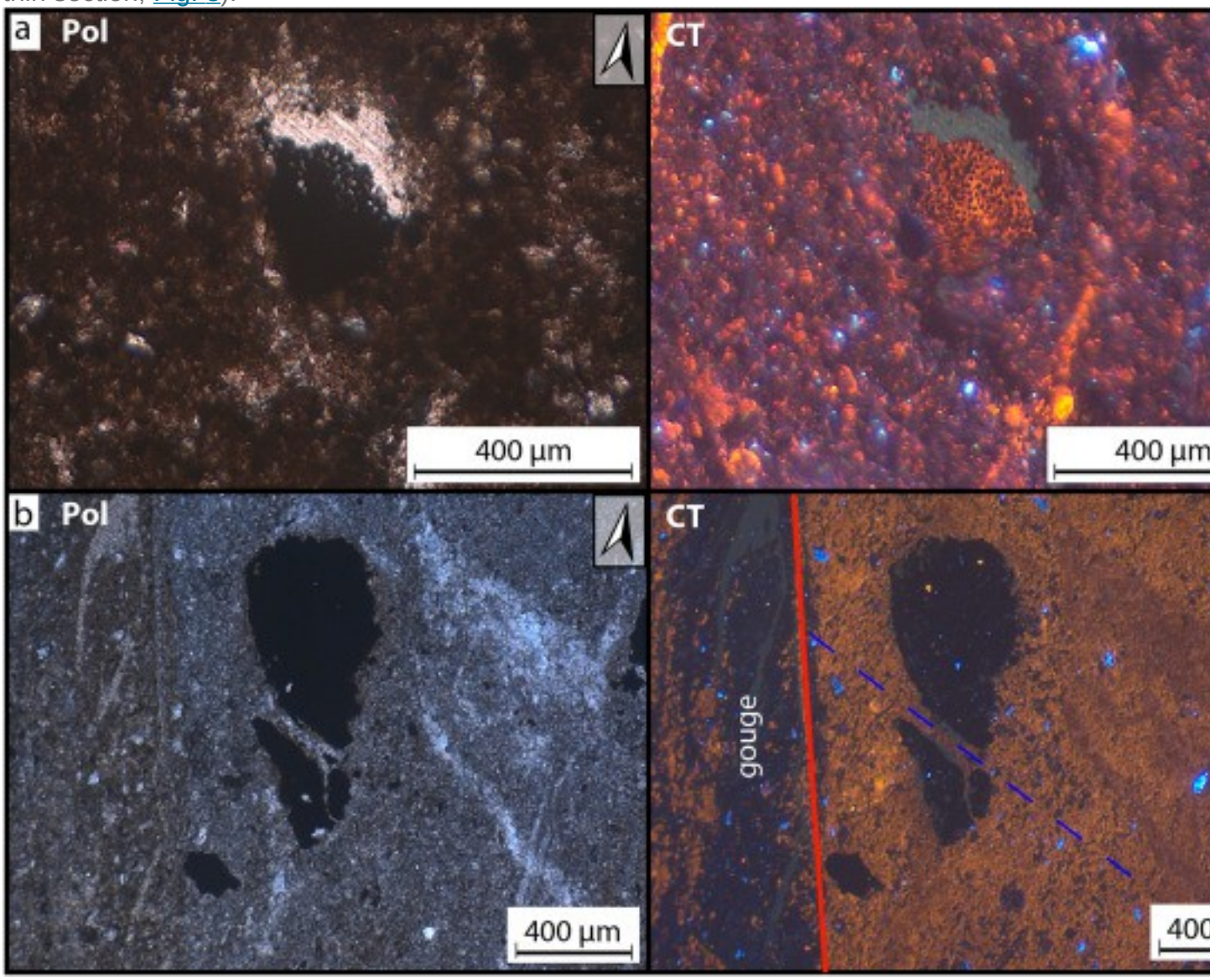

1. Download high-res image (2MB)
2. Download full-size image

Fig. 6. a- Luminescent calcite (C1) fills the pores of framboidal pyrite. b- Analyze from TS3, thin section, in the DZ/FC transition zone, (Fig. 3). Presenting a partly recrystallized pyrite cut by N110°–N120° cracks (dashed blue line) with no apparent

shear displacement. The dark zone (lack of calcite and grain reduction) along a family 3 fault (red line) represent a gouge band. (Pol) is observation with a polarizing microscope and (CL) is cathodo-luminescence observations. (For interpretation of the references to colour in this figure legend, the reader is referred to the web version of this article).

To summarize, the western compartment bearing fractures between intact rock zones, appears characteristic of the fault damage zone deformation texture, while the eastern compartment represents the edge of the damage zone/fault core (DZ/FC) transition zone with brittle/plastic structures and highly fractured residual blocks. Here, this zone corresponds to a 5 cm thick zone where bedding is rotated parallel to the fault surface. Riedel shear are observed, associated with high concentrations of calcite, centimeter scale displacements and dilatant textures such as opening along pre-existing bedding and breccia.

4.2. Episodes of calcite cementation

The views L1 and L2 respectively from thin sections TS1 and TS2 (Fig. 3) show two typical microstructures of the FDZW (Fig. 5). L1 is representative of relatively intact or slightly-deformed rock, composed of carbonates in the form of highly cathodoluminescent and bright orange (in CL) calcite grains, bioclasts, quartz, framboidal pyrite and a dominant fraction of clay minerals. The mineral distribution is relatively homogeneous without any apparent deformation. L2 shows carbonates (mainly high CL calcite cement) concentrating into N010°–N170° and N080°–N100° micro-cracks and fractures while the neighboring clay matrix has fewer calcite grains when compared to L1 (Fig. 5).

L3, L4 and L5 are views (Fig. 5) from the thin section TS3 cut perpendicularly to the central slip surface in the DZ/FC transition zone (Fig. 3). L3 is located in the eastern wall of the central slip surface, a zone where stripes of calcite irregularly alternate with stripes of clay material. Stripes are roughly oriented N160°–N170° and are hundreds of micrometer long. They are sub-parallel to the central fault plane and are cross cut by a N040° left lateral shear fault (associated with f1b, dashed white line in L3, Fig. 5), which could in this context be tentatively interpreted as a R2 shear during the first compression episode, oriented NE–SW. The framboidal pyrite which is located in the bedding plane in the intact rock (L1 sample) here is located in the stripes. This observation suggests that the calcite stripes formed from opening of the bedding and were rotated parallel to the main fault surface (figured by the white continuous lines in L3, Fig. 5) (Fig. 6).

The L4 thin section is located in a brecciated DZ/FC transition zone (Fig. 3). The stripe pattern in L4, appear to be more complex than in L3 as calcite veins more or less surround a partly recrystallized pyrite framboid bearing larger crystals of irregular shape. Luminescent calcite fills the pores in some framboidal pyrites, which also appear altered compared to L1-3 thin sections (Fig. 6a).

The thin section L5 is located close to the f3 shear zone (Fig. 3). There are few shale fragments and quartz grains remaining. Two phases of calcite veins appear, intense CL calcite (C1) being cross-cut by a low luminescent (C2) one (L5, Fig. 5).

C1 luminescence is close to the calcite luminescence observed in the intact shale matrix in thin sections L1 and L2, which could support the hypothesis that C1 originates from the intact shale formation. Likewise, the sigmoid veins indicating a dextral movement, thus presumably formed early in the strike-slip fault history, are composed of the C1.

C2 calcite crosscuts the C1 phase along two main directions. One corresponds to centimeter-thick cracks connecting to the f3 shear planes with an angle of about 20° (dashed green line in L5, Fig. 5, Fig. 7) and then evolving into subparallel secondary planes. The other one corresponds to thin (<0.1 mm) 0.2–0.5 cm cracks making an angle of 120°–130° (dashed blue line in L5, Fig. 5, Fig. 7) with the f3 shear planes (dashed black line in Fig. 7). These N110°–N120° cracks (dashed blue line in L5, Fig. 5, Fig. 7) cut the recrystallized framboidal pyrite with no apparent shear displacement, while the N180°–N020° (green line in L5, Fig. 5, Fig. 7) veins induce a stretching of the pyrite crystals (Fig. 6b).

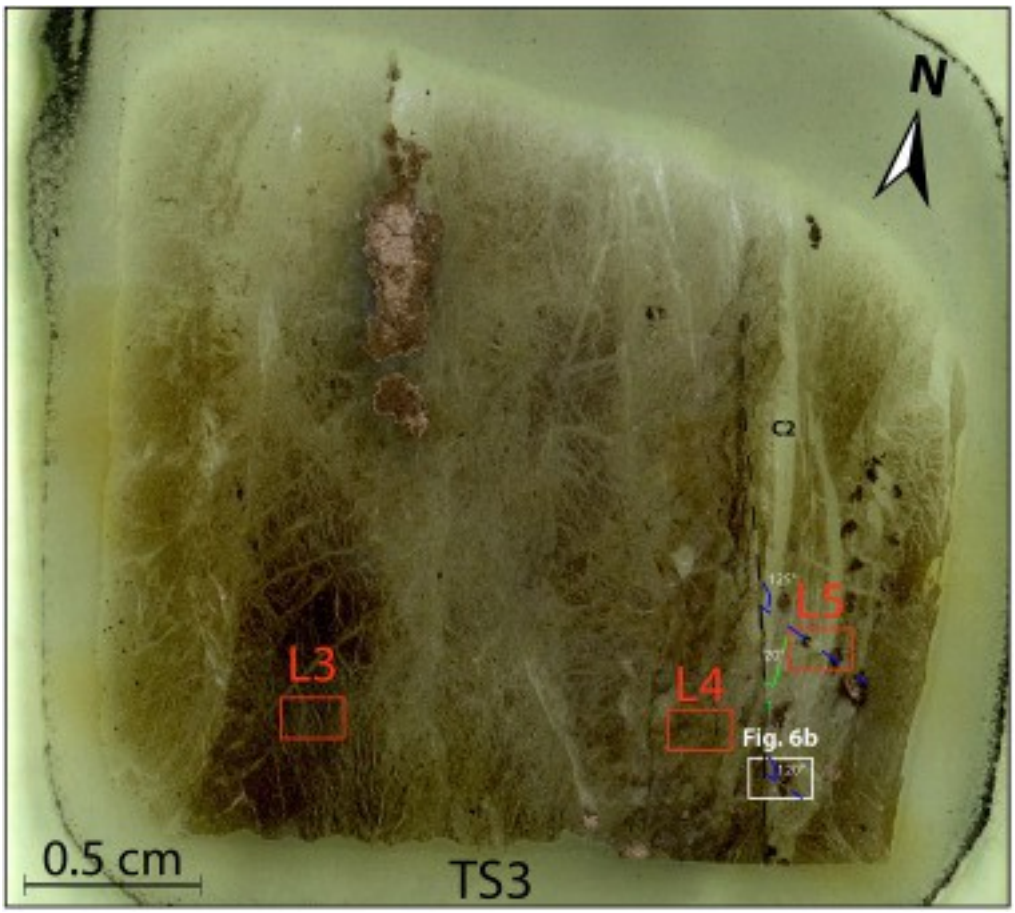

1. Download high-res image (1MB)
2. Download full-size image

Fig. 7. Picture of the TS3 thin section with L3, L4, L5 (presented in Fig. 5) and Fig. 6b.

4.3. Micro-analyses

The main identified chemical elements are Ca, Fe, Zn, S, Si, Al, K, Sr (Fig. 8). The μXRF chemical mapping of three horizontal thin sections along a profile perpendicular to the fault slip surface (Fig. 3, Fig. 8a) shows a difference in the distribution of Ca and Fe in the DZ/FC transition zone (eastern compartment of the sample: μXRF_3, Fig. 3) compared to DZ (western compartment μXRF_1 and μXRF_2). Fig. 8b shows an increase in the Ca (Ca intensity peak × 6) and Fe (Fe intensity peak × 2) concentrations and the appearance of zinc sulphides in the DZ/FC transition zone.

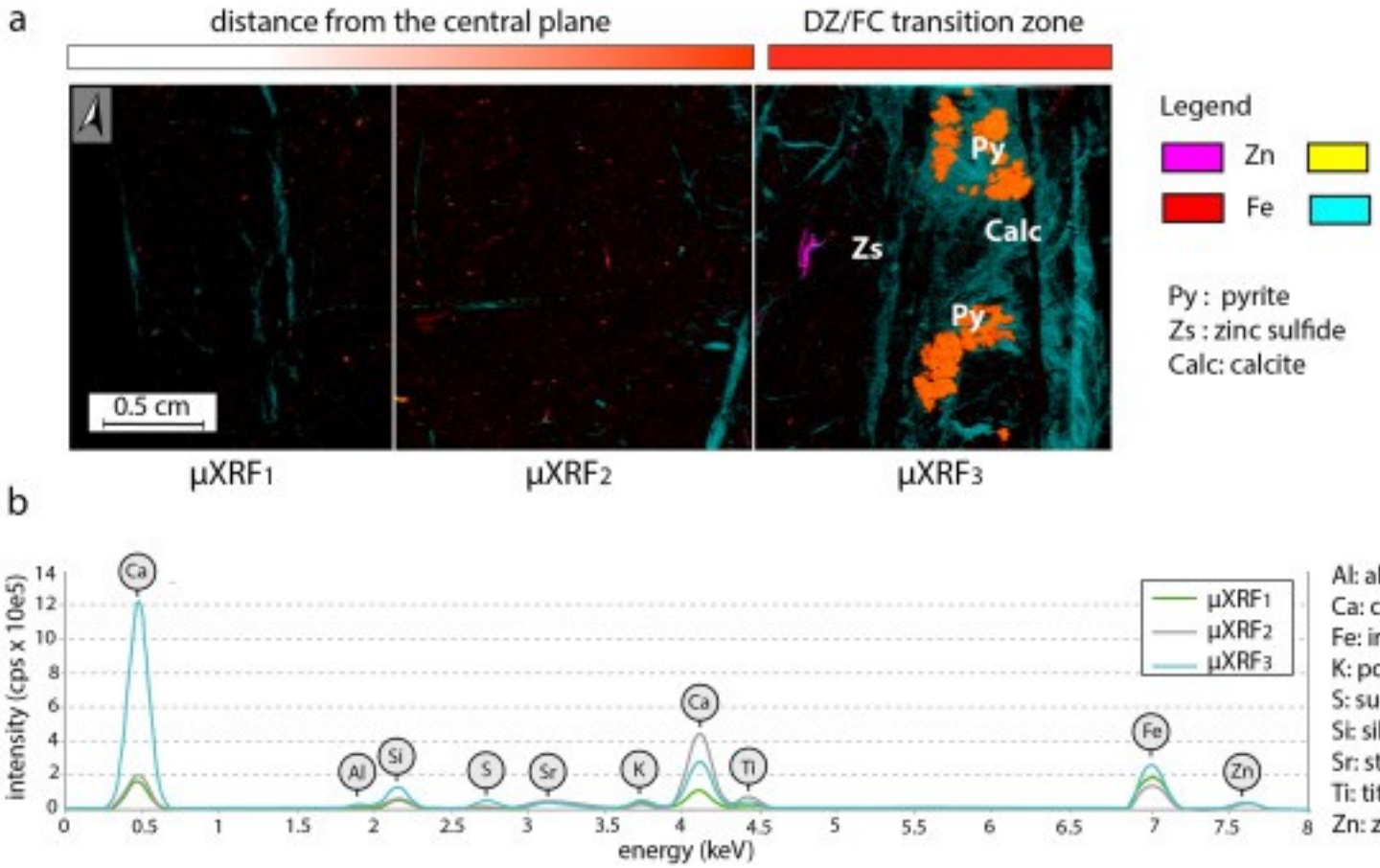

1. Download high-res image (743KB)
2. Download full-size image

Fig. 8. a- µXRF studied zone (1 px = 100 microns, incident: beam: spot 100 microns, 30 kV, anode Rh, counting time: 800 s × 10), μXRF_1 and μXRF_2 are localized in the FDZW and μXRF_3 is localized in the DZ/FC transition zone (see Fig. 3 for locations). b- Mean spectra for each of the μXRF_1, μXRF_2, and μXRF_3 zones showing the chemical variations between the FDZW and the DZ/FC transition zone.

In the damage zone (μXRF_1 and μXRF_2 zones in Fig. 8a), Ca concentrates in f1 faults. Close to the main slip plane (μXRF_3 zone upper right in Fig. 8a), f1 faults are sheared by f3 and f2 faults. In the DZ/FC transition zone, there is a high concentration of diffuse Ca zones affected by veins associated to the f3 shear zones. These shear zones are made of micro-to-millimeter bands of clay minerals and vein shapes are in good accordance with left lateral slip along the shear zones. In details in μXRF_3 zone (bottom east in Fig. 8a), calcite veins appear thicker at the contact with the shear zone, and then evolve into thin calcite veins parallel to the shear zone. The Fe content is diffuse in the damage zone where it corresponds to the small infra-millimeter framboidal pyrite grains, and concentrated in large 0.3–0.5 cm patches of mainly recrystallized pyrite in the

DZ/FC transition zone (Fig. 8a). In μXRF$_3$ zone (lower part), the large patch of pyrite displays a sigmoid shape, showing that pyrite is involved in the shear deformation associated to the f3 slip planes.

5. Interpretation/discussion

5.1. Relationships between vein growth, fluid composition and deformation within the fault zone

Our observations clearly show (Fig. 9): (i) a concentration of calcite in the most deformed part of the DZ/FC transition zone, (ii) two successive calcite precipitation phases associated to different processes of fault deformations and (iii) that slip planes are composed of clay gouge, most calcite veins being located off the slip planes (Fig. 6b). The Fig. 10 highlights two deformation sequences observed in the sample for the two calcite phases; the “Crack + Seal” and the “Crack + Slip + Seal” deformation sequences (Petit et al., 1999).

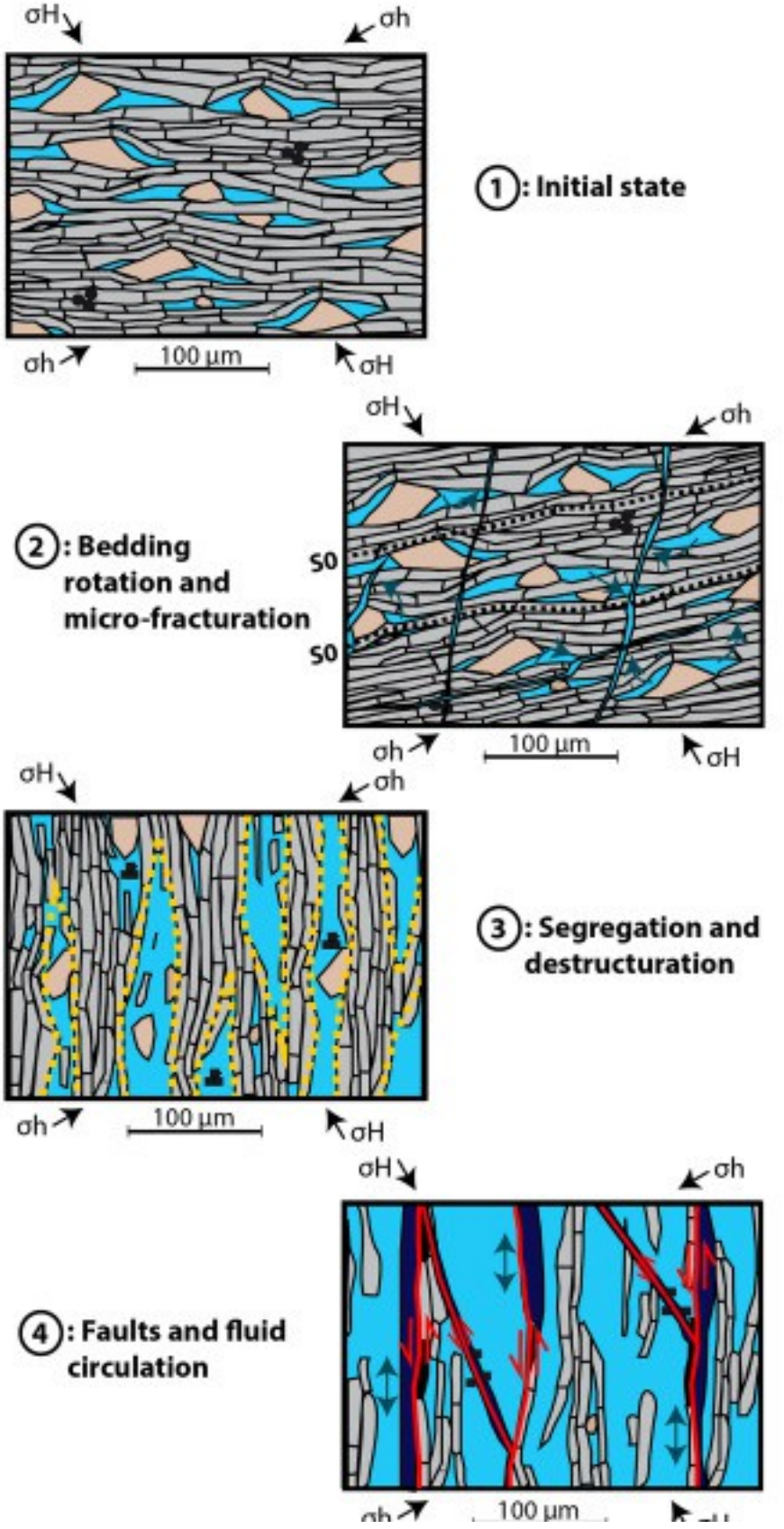
σH
σh
100 µm
①: Initial state
②: Bedding rotation and micro-fracturation
S0
S0
③: Segregation and destructuration
④: Faults and fluid circulation

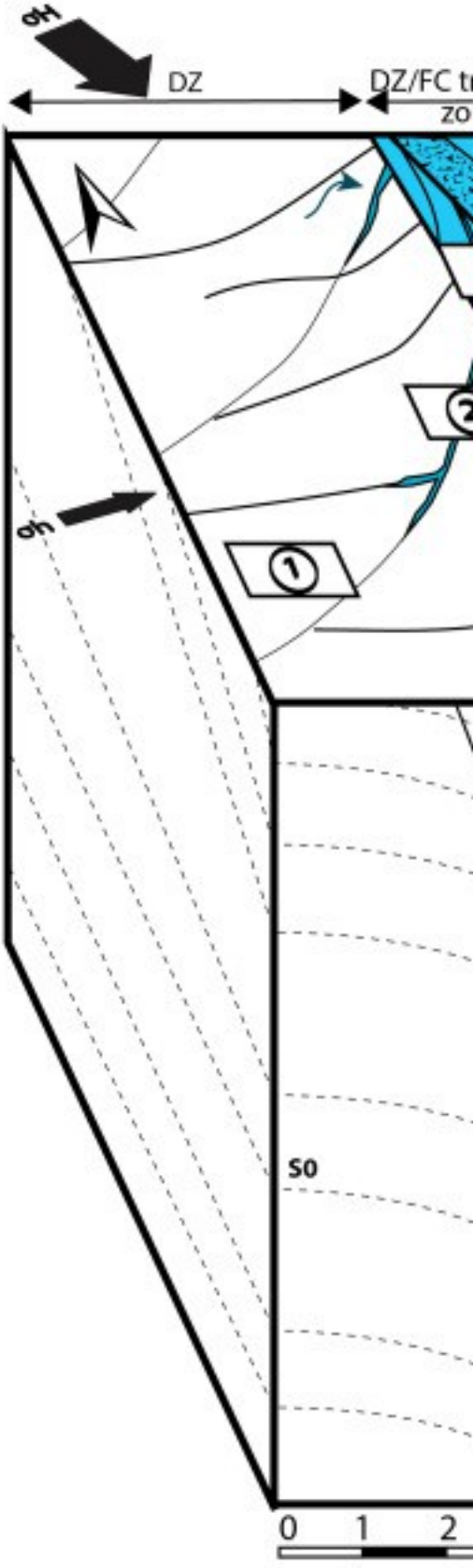
σH
DZ
DZ/FC t
zo
σh
①
②
S0
0
1
2

1. Download high-res image (2MB)
2. Download full-size image

Fig. 9. Synthesis of the coupled paleofluids-strain observations at the Tournemire fault main slip surface. Family 1 fractures have not shown and the fluid proportion is exaggerated in 3 and 4 pictures, for a better visualization.

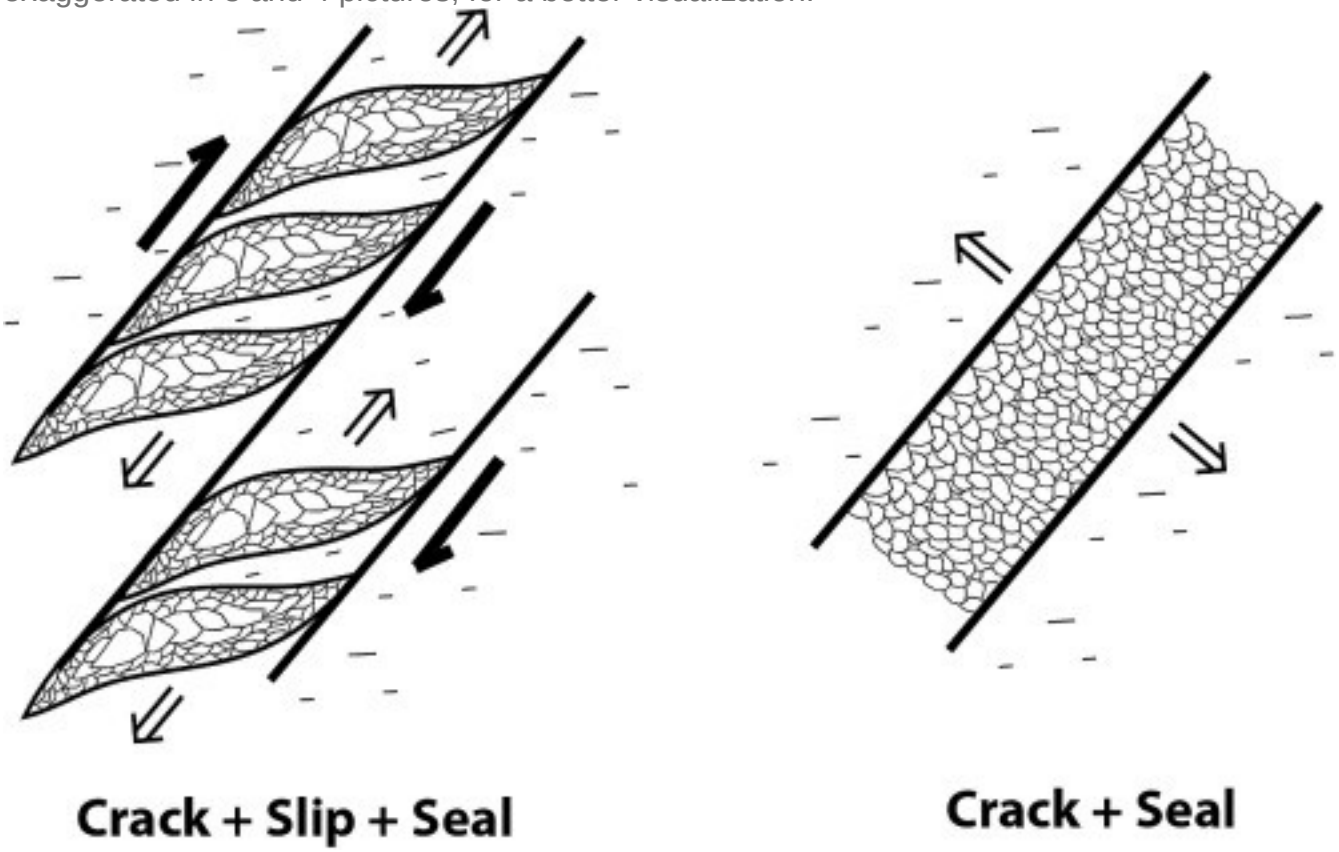

1. Download high-res image (232KB)
2. Download full-size image

Fig. 10. Representation of “crack, then seal” and “crack + slip + seal” deformation sequences.

The first calcite (C1) phase presumably precipitated from a fluid in equilibrium with the formation. It is associated with f1-to-3 fractures in the damage zone, opening of bedding planes and breccification within the fault DZ/FC transition zone. Pyrite recrystallizationoccurs more or less synchronously. The second calcite (C2) phase is associated to late dilation associated with slip on f3 shear zones. It is characterized by sigmoid veins branching from f3 shear zones and small mode 1 cracks. Calcite from this phase displays lower orange luminescence than earlier calcite cements, presumably indicating a lower Mn content (e.g. Cazenave et al., 2003). Some larger crystal of partly recrystallized framboidal pyrite associated with the first

calcite cementation phase have been fractured and these fractures are filled with low luminescence calcite of the second phase. The second phase is thus associated to late shearing and brittle fracturing within a cemented part of the fault core. There is no evidence of pyrite crystallization during this phase.

Peyaud et al. (2006) show that the later calcite cements are formed under less reducing conditions that the earlier cements. The fault zone studied here displays comparable evolution with an earlier episode of high luminescence calcite precipitation and pyrite recrystallization and a later episode of low luminescence calcite precipitation without pyrite recrystallization. We infer the precipitation of these two phases correspond to a similar evolution from more reducing to less reducing conditions and indicate hydrogeologic opening of the system. The later cements represent a comparatively small volume and only occur in association with left lateral slip surfaces. The earlier cements formed during left-lateral slip as well as during an earlier right-lateral episode and possibly also during a syn-sedimentary extensional episode. The hydrogeologic opening of the system occurs relatively late in the faulting history and we wonder whether this opening is the consequence of a better connectivity of the fracture network in the fault zone or the effect of exhumation, erosion and karst development in the overlying formations.

Faults from f1 may be explained by both the state of stresses during the early Basin tectonic inversion and the intact shale anisotropy related to bedding (transverse isotropy). Indeed, according to laboratory tests (Ambrose et al., 2014), if we consider an early upper-cretaceous pulse characterized by N020°–N030° trending horizontal σ1 (Constantin et al., 2004), magnitude over 70 MPa affecting consolidated shales parallel to bedding and a confining stress of about 60 MPa may generate shear rupture surfaces in the shale matrix creating angles of about 20°–30° with the bedding. It could explain the reverse faults N110°–N130° dipping 55°–65°SW and N060°–N080° dipping 60°–80°N. Another explanation of f1 faulting could relate to a Riedel shear zone system, in accordance with an early dextral movement on a pre-existing mean fault plane (during the first NE–SW compression episode).

f2 and f3 faults cross cut f1b and f1c fractures which display an anticlockwise rotation (close to the f3 planes) in good accordance with a left-lateral strike slip reactivation. This reactivation highlights a second compression episode characterized by a N160°–N170 trending horizontal σ1, in good accordance with the principal stress rotation during the second Pyrenean pulse (Constantin et al., 2002, Constantin et al., 2004). The C1 phase is associated with dextral movement of the fault probably during the first episode of the Pyrenean compression (NE–SW) and continued at least during the beginning of the left-

lateral phase, notably associated with breccia formation at the intersections of slip planes. The C2 phase is exclusively associated with the left-lateral reactivation of the fault during the second episode of the Pyrenean compression (SE–NW). The differences between both calcite microstructures may mainly result from the degree of pre-rupture cementation of the fault zone that may alter the fault compliance, the C2 phase affecting already cemented and less compliant fault rocks than the C1 phase.

5.2. Permeability variations during faulting

The distribution of veins in shear zones is controlled by enhanced dilatancy along releasing segments of the shear zones, which may channel fluid flow and eventually contribute to resealing the fault by calcite precipitation. Different ways of potential permeability increase related to dilation induced by fault movements affecting shales are observed in the studied block. Most dilation occurs at a distance from the main slipping planes. Patches of brecciated shale with high fracture porosity formed around the intersections between the main shear planes and secondary faults (e.g. R1) or inherited structures such as re-oriented bedding or small faults formed in a different stress regime. Interestingly, these high dilatant zones take place in relatively low strain areas, in the transition zone between the damage zone and the fault core. In this case study, the zone containing potential high permeability conduits for flow is a few centimeters-thick. During the reactivation phase the same dilatant effects may occur much more localized close to a few active shear planes with clay gouge. This is in accordance with permeability tests conducted during laboratory shear tests on a sample pre-cut by a fracture that showed series of fractures and a complex pattern of deformation occurring off the slipping fracture surface to a distance of about 1 mm (Cuss et al., 2011). In addition, Bolton et al. (1999) showed that after being deformed at a high over-consolidation ratio, shear zones in fine-grained sediments can dilate and thereby act as efficient fluid-flow conduits. In the Tournemire shales, both over-consolidation under a high burial stress and calcite sealing may have produced the conditions for brittle dilatant failure in shear and a potentially strong permeability-vs-stress dependency.

6. Conclusions

The micro-structural and chemical analyses of a block sample from a fault zone intersected in the Tournemire URL, indicate two calcification phases took place. The fault zone recorded two episodes of compressive deformation during the Pyrenean orogeny along NE–SW and SE–NW directions that result in the formation of both right lateral and left lateral shear structures, the latter being more developed in the

block studied. We show that the first calcite phase has fossilized fluids channels conditioned by the brittle dilatant behavior of the anisotropic intact shales under moderate confining stress. Then, sealing of the initial fault zone structures occurred, conditioning much more localized and comparatively less dilatant strain during a late episode of left-lateral slip (Fig. 9). Our observations indicate that dilation occurs in a wider zone during fault initiation (all the studied block is affected) or at least when strain was not localized on discrete slipping surface, than when the fault is reactivated along a main shear plane at the boundary of the fault core. In any case, most dilation occurs off the main shear planes, and is primarily associated to interaction between structures, either pre-existing like bedding or early fractures, or coevolving such as Reidel shears.

Although dilation, as indicated by vein volume, appears more developed during the early stages of deformation, the coeval recrystallization of pyrite suggests the prevalence of reducing conditions. The later opening of the hydrogeological system to more oxidizing conditions is probably the result of a better hydraulic connectivity of the system during later stages of fault activity.

Acknowledgments

The authors would like to thank Total for funding (contract FR00006163) and IRSN to allow access to the Tournemire laboratory facility and their help and participation to the experiments. This study was also financially supported by CNRS program NEEDS-MIPOR (PFAAT). We also would like to thank Lionel Marié for the thin sections and samples realization and Perrine Chaurand for the use of the XRF analysis.

References

Ambrose et al., 2014

J. Ambrose, R.W. Zimmerman, R. Suarez-Rivera**Failure of Shales under Triaxial Compressive Stress**

American Rock Mechanics Association (2014), pp. 14-7506

View Record in Scopus

Arch and Maltman, 1990

J. Arch, A. Maltman**Anisotropic permeability and tortuosity in deformed wet sediments**

J. Geol. Res., 95 (B6) (1990), pp. 9035-9045

CrossRefView Record in Scopus

Barbarand et al., 2001

J. Barbarand, F. Lucazeau, M. Pagel, M. Séranne**Burial and exhumation history of the south-eastern Massif Central (France) constrained by apatite fission-track thermochronology**

Tectonophysics, 335 (2001), pp. 275-290
ArticleDownload PDFView Record in Scopus

Berg and Skar, 2005
S.S. Berg, T. Skar**Controls on damage zone asymmetry of a normal fault zone: outcrop analyses of a segment of the Moab fault, SU Utah**
J. Struct. Geol., 27 (2005), pp. 1803-1822
ArticleDownload PDFView Record in Scopus

Billi et al., 2003
A. Billi, F. Salvini, F. Storti**The damage zone-fault core transition in carbonate rocks: implication for fault growth, structure and permeability**
J. Struct. Geol., 25 (2003), pp. 1779-1794
ArticleDownload PDFView Record in Scopus

Blès et al., 1989
J.L. Blès, D. Bonijoly, C. Castaing, Y. Gros**Successive post-Variscan stress fields in the French Massif Central and its borders (Western European plate): comparison with geodynamic data**
Tectonophysics, 169 (1989), pp. 79-111
ArticleDownload PDFView Record in Scopus

Bretaudeau et al., 2014
F. Bretaudeau, C. Gélis, D. Leparoux, R. Brossier, J. Cabrera, P. Côte**High-resolution quantitative seismic imaging of a strike-slip fault with small vertical offset in clay rocks from underground galleries: experimental platform of Tournemire, France**
Geophysics, 79 (1) (2014), pp. B1-B18
CrossRef

Bonin, 1998
B. Bonin**Deep geological disposal in argillaceous formations: studies at the Tournemire test site**
J. Contam. Hydrol., 35 (1998), pp. 315-330
ArticleDownload PDFView Record in Scopus

Boisson et al., 2001
J.Y. Boisson, L. Bertrand, J.F. Heitz, Y. Moreau-Le Golvan**In situ laboratory investigations of fluid flow through an argillaceous formation at different scales of space and time, Tournemire tunnel, southern France**
Hydrogeol. J., 9 (2001), pp. 108-123
CrossRefView Record in Scopus

Bolton et al., 1999
J. Bolton, B. Clennell, J. Maltman**Nonlinear stress dependence of permeability: a mechanism for episodic fluid flow in accretionary wedges**
March 1999

Geology, 27 (3) (1999), pp. 239-242
3 figures
CrossRefView Record in Scopus

Bonijoly and Delpont, 1982

D. Bonijoly, G. Delpont**Etude du bassin des Causses et de la bordure cévenole par la télédétection et la géologie structurale**
BRGM Orléans, 46 (1982), p. 64
View Record in Scopus

Bruhn et al., 1994

R.L. Bruhn, W.T. Parry, W.A. Yonkee, T. Thompson**Fracturing and hydrothermal alteration in normal fault zones**
Pure Appl. Geophys., 142 (1994), pp. 609-644
CrossRefView Record in Scopus

Cabrera et al., 1999

J. Cabrera, P. Volant, C. Baker, W. Pettitt, R.P. Young**Structural and geophysical investigations of the EDZ (excavation disturbed zone) in indurated argillaceous media: the tunnel and the galleries of the IPSN Tournemire site (France)**
Vail, Amadei, Kranz, Scott, Smeallie (Eds.), 37th U.S Rock Mechanics Symposium, Balkema (1999), pp. 957-964
View Record in Scopus

Caine et al., 1

9
9
6

J.S. Caine, J.P. Evans, C.B. Forster**Fault zone architecture of permeability structure**
Geology, 24 (1996), pp. 1025-1028
CrossRefView Record in Scopus

Cazena
ve et al.,
2003

S. Cazenave, R. Chapoulie, G. Villeneuve**Cathodoluminescence of synthetic and natural calcite: the effects of manganese and iron on orange emission**
Mineral. Petrol., 78 (2003), pp. 243-253
CrossRefView Record in Scopus

Charpentier
et al., 2003

D. Charpentier, D. Tessier, M. Cathelineau**Shale microstructure evolution due to tunnel excavation after 100 years and impact of tectonic paleo-fracturing. Case of Tournemire, France**
Eng. Geol., 70 (2003), pp. 55-69
ArticleDownload PDFView Record in Scopus

Chester and Log
1986

F.M. Chester, J.M. Logan**Implications for mechanical properties of brittle faults from observations of the Punchbowl fault zone, California**
Pure Appl. Geophys., 124 (1986), pp. 79-106
CrossRefView Record in Scopus

Chester et al., 19

F.M. Chester, J.P. Evans, R.L. Biegel**Internal structure and weakening mechanisms of the San Andreas fault**
J. Geophys. Res., 98 (1993), pp. 771-786
CrossRefView Record in Scopus

Clausen et al., 2

J.A. Clausen, R.H. Gabrielsen, E. Johnsen, J.A. Korstgard**Fault architecture and clay smear distribution. Examples from field studies and drained ring-shear experiments**
Nor. J. Geol., 83 (2003), pp. 131-146
View Record in Scopus

Constantin et al.

J. Constantin, P. Vergély, J. Cabrera**Tectonique et fracturation associée dans le bassin des Causses (Aveyron, France): le cas du secteur de Tournemire**

Bull. Soc. Géol. Fr., 173 (3) (2002), pp. 229-243
CrossRefView Record in Scopus

Constantin, 2002

J. Constantin**Fracturat ion et paléocirculation de fluides dans les formations géologiques de faible perméabilité matricielle: le cas des argilites de Tournemire (Aveyron, France)**
Thèse
Université d'Orsay, France (2002)

Constantin et al.

J. Constantin, J.B. Peyaud, P. Vergély, M. Pagel, J. Cabrera**Evolution of the structural fault permeability in argillaceous rocks in a polyphased tectonic context**
Phys. Chem. Earth, 29 (2004), pp. 25-41
ArticleDownload PDFView Record in Scopus

Constantin et al.

J. Constantin, P. Laurent, P. Vergély, J. Cabrera**Paleo-deviatoric stress magnitudes from calcite twins and related structural permeability evolution in minor fault: example from the toarcian shale of the French Causses Basin, Aveyron, France**
Tectonophysics, 429 (2007), pp. 79-97
ArticleDownload PDFView Record in Scopus

Cornet, 2000

F.H. Cornet**Détermination du champ de contrainte au voisinage du laboratoire souterrain de Tournemire. Rapport du Laboratoire de Mécanique des Roches**
Département de Sismologie, Institut de Physique du Globe de Paris (2000)

Courbet et al., 20

C. Courbet, P. Dick, M. Lefèvre, C. Witterbroodt, J. Matray, J. Barnichon**Estimating Hydraulic Conductivities in a Fractured Shale Formation from Pressure Pulse Testing and 3d Modeling**
American Geophysical Union (2013)
Fall Meeting 2013, abstract #MR11A-2202

Cuss et al., 2011

R.J. Cuss, A. Milodowski, J.F. Harrington**Fracture transmissivity as a function of normal and shear stress: firs results in opalinus clay**
Phys. Chem. Earth, 36 (2011), pp. 1960-1971
ArticleDownload PDFView Record in Scopus

De Charpal et al

O. De Charpal, P. Trémonlière, Jean, P. Masse**Un exemple de tectonique de plate-forme: les Causses majeurs (sud du Massif central)**
Rev. IFP, 5 (XXIX) (1974), pp. 641-659
View Record in Scopus

Devès et al., 201

G. Devès, A.-S. Perroux, T. Bacquart, C. Plaisir, J. Rose, S. Jaillet, B. Ghaleb, R. Ortega, R.Mair e**Chemical element imaging for speleothem geochemistry: application to a uranium-bearing corallite with aragonite diagenesis to opal (Eastern Siberia, Russia)**
Chem. Geol., 294–295 (2012), pp. 190-202
ArticleDownload PDFView Record in Scopus

Dick et al., 2015

P. Dick, C. Courbet, C. Wittebrood, A. Dauzere, J.-M. Matray**Internal structures of fault zones in low permeability formation and their relationship with fluid flow: insights the Tournemire URL**
Clay in Natural and Engineered Barriers for Radioactive Waste Confinement (2015)
Bruxelle. Abstract 15–21

Evans et al., 199

J.P. Evans, C.B. Forster, J.V. Goddard**Permeability of fault-related rocks, and implications for implications for hydraulic structure of fault zones**
J. Struct. Geol., 19 (1997), pp. 1393-1404
ArticleDownload PDFView Record in Scopus

Faulkner et al., 2

D.R. Faulkner, A.C. Lewis, E.H. Rutter**On the internal structure and mechanics of large strike-slip fault zones: field observations of a Carboneras fault in southeastern Spain**
Tectonophysics, 367 (2003), pp. 235-251
ArticleDownload PDFView Record in Scopus

Faulkner et al., 2

D.R. Faulkner, C.A.L. Jackson, R.J. Lunn, R.W. Schlische, Z.K. Shipton, C.A.J. Wibberley**A revie w of recent developments concerning the structure, mechanics and fluid flow properties of fault zone**
J. Struct. Geol., 32 (2010), pp. 1557-1575
ArticleDownload PDFView Record in Scopus

Gudmundsson e

A. Gudmundsson, S.S. Berg, K.B. Lyslo, E. Skurtveit**Fracture networks and fluid transport in active fault zones**
J. Struct. Geol., 23 (2001), pp. 343-453
View Record in Scopus

Gudmunson et a

A. Gudmunson, T.H. Simmenes, B. Larsen, S.L. Philipp**Effects of internal structure and local stresses on fracture propagation, deflection, and arrest in fault zones**
J. Struct. Geol., 32 (2010), pp. 1643-1655

Hesthammer et a

J. Hesthammer, T.E.S. Johansen, L. Watts**Spatial relationships within fault damage zones in sandstone**

Mar. Pet. Geol., 17 (2000), pp. 873-893
ArticleDownload PDFView Record in Scopus

Jourde et al., 20

H. Jourde, E.A. Flodin, A. Aydin, L.J. Durlofski, X.H. Wen**Computing permeability of fault zones in eolian sandstone from outcrop measurement**
AAPG Bull., 86 (2002), pp. 1187-1200
View Record in Scopus

Kim et al., 2004

Y.S. Kim, D.C.P. Peacock, D.J. Sanderson**Fault damage zones**
J. Struct. Geol., 26 (2004), pp. 503-517
ArticleDownload PDFView Record in Scopus

Mandl et al., 197

G. Mandl, L.N.J. Jong, A. Maltha**Shear zones in granular materiel, an experimental study of their structure and mechanical genesis**
Rock Mech., 9 (1977), pp. 95-144
CrossRefView Record in Scopus

Manzocchi et al.

T. Manzocchi, J.J. Walsh, P. Nell, G. Yielding**Fault transmissibility multipliers for flow simulation models**
Pet. Geosci., 5 (1999), pp. 53-63
CrossRefView Record in Scopus

Martin and Berge

P. Martin, F. Bergerat**Palaeo-stresses inferred from macro- and microfractures in the Balazuc-1 borehole (GPF programme). Contribution to the tectonic evolution of the Cévennes boreder of the SE Basin of France**
Mar. Pet. Geol., 13 (6) (1996), pp. 671-684
ArticleDownload PDFView Record in Scopus

Nussbaum et al.

C. Nussbaum, P. Bossart, F. Amann, C. Aubourg**Analysis of tectonic structures and excavation induced fractures in the opalinus clay, Mont Terri underground rock laboratory (Switzerland)**
Swiss. J. Geosci., 104 (2011), pp. 187-210, 10.1007/s00015-011-0070-4
CrossRefView Record in Scopus

Nussbaum and B

C. Nussbaum, P. Bossart**Compilation of K-values from Packer Tests in the Mont Terri Rock Laboratory**
Technical Note 2005-10, Mont-Terri Project
Geotechnical Institute Ltd, Switzerland (2004)

Petit et al., 1999

J.-P. Petit, C.A.J. Wibberley, G. Ruiz**Crack-seal, slip: a new fault valve mechanism?**
J. Struct. Geol., 21 (1999), pp. 199-1207

Peyaud et al., 20

J.B. Peyaud, J. Barbarand, A. Carter, M. Pagel**Mid-Cretaceous uptift and erosion on the northern margin of the Ligurian Tethys deduced from thermal history reconstruction**
Int. J. Earth Sci., 94 (2005), pp. 462-474
CrossRefView Record in Scopus

Peyaud et al., 20

J.B. Peyaud, M. Pagel, J. Cabrera, H. Pitsch**Mineralogical, chemical and isotopic perturbations induced in shale by fluid circulation in a fault at the Tournemire experimental site (Aveyron, France)**
J. Geochem. Explor., 90 (2006), pp. 9-23
ArticleDownload PDFView Record in Scopus

Rice and Rudnic

J.R. Rice, J.W. Rudnicki**Earthquake precursory effects due to pore fluid stabilization of a weakening fault zone**
J. Geophys. Res., 84 (B5) (1979), pp. 2177-2193, 10.1029/JB084iB05p02177
CrossRefView Record in Scopus

Séranne et al., 2002

M. Séranne, H. Camus, F. Lucazeau, J. Barbarand, Y. Quinif**Surrection et érosion polyphasées de la bordure cévenole – Un exemple de morphogenèse lente**
Bull. Soc. Géol. Fr., 173 (2) (2002), pp. 97-112
CrossRefView Record in Scopus

Séranne, 2014

M. Séranne**Y a-t-il du gaz de schiste en Languedoc?**
Ann. Soc. d'Hortic. d'Hist. Nat. l'Héranlt, 154 (2014)

Sibson, 1977

R.H. Sibson**Fault rock and fault mechanisms**
J. Geol. Soc., 133 (1977), pp. 191-213
CrossRefView Record in Scopus

Tremosa et al., 2012

J. Tremosa, D. Arcos, J.M. Matray, F. Bensenouci, E.C. Gaucher, C. Tournassat, J. Hadi**Geoche mical characterization and modelling of the Toarcian/Domerian porewater at the Tournemire underground research laboratory**
Appl. Geochem., 27 (2012), pp. 1417-1431
ArticleDownload PDFView Record in Scopus

Wibberley et al., 2008

C.A.J. Wibberley, G. Yielding, G. Di Toro**Recent advances in the understanding of faul zone internal structure: a review. The internal structure of fault zones**

Geol. Soc. Lond., 299 (2008), pp. 5-33

CrossRefView Record in Scopus

Yielding et al., 1999

G. Yielding, J.A. Øverland, G. Byeberg**Characterization of fault zones for reservoir modeling: an example from Gullfaks Field, Northern North Sea**

Am. Assoc. Pet. Geol. Bull., 83 (1999), pp. 925-951

View Record in Scopus

Zhang and Cox, 2000

S. Zhang, S.F. Cox**Enhancement of fluid permeability during shear deformation of a synthetic mud**

J. Struct. Geol., 22 (2000), pp. 1385-1393

ArticleDownload PDFView Record in Scopus